ELSEVIER

Journal of Crystal Growth 237–239 (2002) 2082–2090

JOURNAL OF CRYSTAL GROWTH

www.elsevier.com/locate/jcrysgro

Study of impurity segregation, crystallinity, and detector performance of melt-grown cadmium zinc telluride crystals

M. Schieber[a,*], T.E. Schlesinger[b], R.B. James[c], H. Hermon[d], H. Yoon[e,1], M. Goorsky[e]

[a] *Graduate School of Applied Science, Hebrew University of Jerusalem, Jerusalem 91904, Israel*
[b] *Carnegie Mellon University, Pittsburgh, PA 15213, USA*
[c] *Brookhaven National Laboratory, Upton, NY 11973-5000, USA*
[d] *Real Time Radiography Readout, Malkha Technological Park, Jerusalem 91487, Israel*
[e] *University of California at Los Angeles, Los Angeles, CA 90024, USA*

Abstract

A review of growth methods used to produce $Cd_{1-x}Zn_xTe$ (CZT) $(0.0<x<0.20)$ crystals for radiation detector applications is presented. Most of the results emphasize the high-pressure Bridgman (HPB) method. For selected melt-grown HPB ingots, the liquid/solid segregation coefficients of some impurities were measured. The correlation of the impurity content and nuclear detector performance will be discussed. Extended defects and surface and bulk crystallinity were measured using triple and double axis X-ray diffraction techniques (TAD and DAD XRD), X-ray topography, and infrared microscopy. X-ray diffraction maps and IR images were generated and compared to gamma-ray detector tests to correlate macroscopic defects with the nuclear detector responses. Defects states of CZT were also investigated using low-temperature photoluminescence spectroscopy. Comparisons between the material and detector properties for different CZT growth methods will be discussed.

PACS: 07.85.NC; 72.80.EY

Keywords: A1. X-ray topography; A2. Growth from melt; B1. Zinc compounds; B2. Semiconducting II–VI materials

1. Introduction

The cubic zincblende structure of $Cd_{1-x}Zn_xTe$ (CZT) with $(0\leqslant x\leqslant 0.2)$ has an important combination of the desired properties necessary to fabricate a room temperature-operating nuclear radiation detector. These properties are: (1) band gap energy above 1.5 eV to control thermally generated current and resultant losses in energy resolution; (2) high atomic number of the constituent elements for high photon interaction; (3) mechanical strength; (4) freedom from polarization effects; (5) ability to grow high-resistivity crystals; (6) photosensitivity; and (7) relatively good charge transport properties [1]. Another important requirement is the commercial availability, which currently exists from several vendors in the USA, Ukraine and Israel. The present paper will review the current status of the CZT material

*Corresponding author. Tel.: +972-2-658-4364; fax: +972-2-566-3878.
E-mail address: schieber@vms.huji.ac.il (M. Schieber).
[1] Present Address: Spectrolab, Sylmar, CA 91342, USA.

0022-0248/02/$ - see front matter
PII: S0022-0248(01)02314-4

used for X-ray and gamma-ray detector and imaging applications.

2. Crystal Growth

Attempts to grow CZT from the vapor phase [2,3] have so far not produced spectrometer quality crystals; therefore, the results reported in this paper will concentrate on melt-grown material. CdTe and ZnTe form a solid solution throughout the entire alloy range and temperature-composition phase diagram [4]. For production of nuclear detectors the composition range of interest is $0.0 < x < 0.2$. Higher Zn compositions ($x > 0.2$) have been investigated, but the transport properties were poorer compared to crystals with lower Zn compositions.

A number of methods have been successfully employed in the growth of $Cd_{1-x}Zn_xTe$ particularly for the composition range of $x = 0.04$, which is widely used as a substrate for epitaxial growth of HgCdTe for infrared detector applications. Some of the CZT materials grown as IR substrates were also studied as nuclear detectors.

The traveling wave heater [5] and several variations of the Bridgman method are discussed [6,7]. However, for room temperature radiation detectors, the most commonly used method, with few exceptions, has been the high-pressure Bridgman (HPB) process [8–12]. The HPB method is used by most current commercial suppliers including those in Russia and the Ukraine. Many papers reporting the material and detector properties can be found in the literature (see, for example, Refs. [13–21]).

The basic Bridgman method involves the movement of a crucible containing the melt through a furnace designed to provide a suitable temperature profile. The furnace may be either vertical or horizontal. The crucible may be transported through the heater, or alternatively the furnace can be held stationary and the temperature profile altered. In the HPB method, an excess pressure of 10–150 atm of an inert gas, typically argon, is maintained over the melt to suppress the loss of volatile components [22]. While the elevated pressure reduces the loss of these components, the losses are not eliminated. Continuous loss of cadmium, the highest vapor pressure component, causes the melt to become enriched in tellurium as the growth proceeds. The HPB furnace is enclosed in a steel pressure vessel. The temperature profile of the furnace is maintained by graphite, Kanthal [23] or other heater elements and monitored with internal thermocouples. A multi-zone temperature profile is preferred with the hot zone fixed at about 1100°C. The crucible is fitted with a cover to reduce vapor losses. Particular care must be taken in the choice of crucible material because of the potential for contamination of the melt. Quartz, for example, can be a source of significant oxygen contamination. Porous graphite, which is amenable to high-temperature bake out, is used most frequently, although pyrolytic boron nitride has also been utilized [24]. The movement of the crucible is controlled by a mechanical actuator introduced through a high-pressure feedthrough. Crucibles with inside diameters up to 10 cm holding charges up to 10 kg have been reported [9]. Growth rates vary, but they are typically in range of 0.1–1 mm/h. Recently, some good results for preparation of nuclear detectors have also been obtained using low-pressure Bridgman, both in horizontal and vertical geometries [25–26]. Data on low-pressure Bridgman grown samples will also be presented and discussed in this paper.

In practice, the constituent elements undergo multiple purification, and they are weighed to stoichiometric proportions before introduction into the crucible. Dopants such as aluminum [27] are intentionally introduced to compensate the crystals. Prior to initiation of the growth cycle, the charge is heated following a programmed schedule. After the growth phase the crystal is gradually cooled to room temperature, and the vessel is brought to ambient pressure. The complete growth cycle is completed in about 2–4 weeks.

3. Impurity analyses and segregation coefficient

In order to compensate for the effects of Cd vacancies caused by the evaporation of Cd during growth, several dopants have been tried, such as In

Table 1
Elemental analysis results of slices cut along three CZT ingots (ppmw)

Distance from origin (nm)	Li	Mg	Al	Si	S	Ca	Cr	Mn	Fe	Cu	Ga	Se
CZT (Al doped)												
62	0.048	0.24	820	11	1.6	12	0.54	0.14	6.5	0.89	1.9	0.58
46	0.001	0.75	435	0.11	0.29	0.21	0.009	0.28	2.4	0.049	0.25	0.13
30	0.006	9.3	1115	15	0.98	0.32	0.029	0.041	0.86	0.081	0.2	0.7
6	0.01	0.47	450	0.02	0.84	0.041	0.021	0.088	1	0.036	0.42	0.69
CZT (undoped)												
62	0.035	0.35	25	0.6	0.088	12	1.5	0.42	165	0.4	0.02	0.67
46	0.001	0.066	0.55	0.028	0.034	0.009	0.007	0.12	14	0.033	0.01	0.64
30	0.001	0.11	1.4	0.037	0.012	0.005	0.005	0.12	6.7	0.005	0.01	0.006
6	0.001	0.066	0.12	0.007	2.8	0.008	0.003	0.002	0.41	0.031	3.5	2.2

and Al. However, adding dopants may change the distribution of other impurities, as well as create new trapping centers. Chemical analyses of some specially doped HPB-CZT were made using glow discharge mass spectrometry [28]. Some typical results measured on Al doped and on undoped samples are shown in Table 1. Chemical analyses in the ppbw region may not be accurate enough to allow the determination of the segregation coefficients, but an attempt was made to determine approximate values for these coefficients.

Details of the calculations of the segregation coefficients K_i are given elsewhere [29]. The results are shown in Table 2. The values should be considered as rough approximations due to problems with precise elemental quantification, contamination during growth, impurity diffusion in the solid during growth and cool-down, contamination during processing and handling, and imperfect fits based on the limited number of data points along the growth axis.

One can see that the impurity distribution is changed between the undoped and Al doped sample, particularly for Si, S, and Fe. The values of K_i are also changed.

An analysis of the same impurities performed on vapor-grown crystals shows a lower content of impurities by up to 2 orders of magnitude, however, their nuclear spectroscopic performance is much worse than the samples grown by HPB. This observation suggests that stoichiometry might play a critical role in limiting the carrier lifetime in CZT crystals, since the stoichiometry of melt- and vapor-grown material is expected to differ substantially.

Table 2
Segregation coefficients for different impurities measured on Al doped and undoped CZT ingots

Impurity	Segregation coefficient			
	Undoped		Al doped	
	K	C_0 (ppmw)	K	C_0 (ppmw)
Li	0.088	0.00	0.049	0.012
Mg	0.29	0.17	0.65	0.679
Al	0.016	2.96	0.73	537
Si	0.021	0.19	0.018	2.22
S	3.2	1.28	0.9	0.784
Ca	0.028	0.28	0.0056	3.43
Cr	0.007	0.08	0.065	0.152
Mn	0.008	0.16	0.53	0.113
Fe	0.006	39.9	0.28	2.76
Cu	0.038	0.06	0.070	0.291
Ga	0.43	0.01	0.41	0.484
Se	1.61	1.41	1.50	0.457

4. Macro-defects in CZT

Among the most commonly found macro-defects present in the CZT crystals are pipes, wires, cracks, grain and twin boundaries as well as tellurium inclusions. The cracks are usually filled with Te and carbon, as analyzed using X-ray energy dispersive spectroscopy [29]. The graphite crucible can be the source of carbon, although

infiltration of the cutting oils during slicing may be the primary source of the carbon. The Te precipitates result from retrograde solubility in the phase diagram, and they are inherent in the HPB process. Post-growth annealing can be used to alter the concentration and size of the precipitates. The spatial distribution is normally one of three types: dispersed, cellular, or segregated along the grain and twin boundaries. Those precipitates dispersed in CZT have been reported to have little effect on the electrical properties [10]. However, simple models based on the common anion rule and band offsets suggest that the precipitates will act as electron traps. Te precipitates along the grain and twin boundaries are one of the gross defects affecting the detector performance, particularly for multi-element imaging arrays. The Te-rich precipitates present along the grain boundaries and twins increase the dark current of the CZT detector and reduce the charge collection properties. Due to the relatively low band gap (0.33 eV) of Te, the electrical resistivity of the precipitates will be several orders of magnitude lower than the surrounding CZT and might account for the higher leakage found along grain boundaries. Impurities may also have an affinity for these sites, and they could contribute to the degraded electrical and transport properties as well. An infrared transmission micrograph of Te precipitates along a grain boundary shown in Fig. 1. The net result of the various macro-defects is to limit the useful portion of currently available HPB ingots to about 25% of the total volume [10]. Furthermore, the size of the detectors produced from single CZT crystals is limited by the boundaries. Some of the problems with relatively small single crystals have been overcome by using conventional Bridgman techniques.

In addition to the defects noted above, there are effects related to liquid–solid solubility factors, which manifest as axial (along growth axis) variations in the concentration of both impurities and the base constituents of Cd, Zn and Te. Of particular importance is the decline in the zinc concentration along the growth axis of the boule due to its segregation coefficient being >1. A practical consequence of the Zn distribution is that detectors made from material cut along the growth axis will have band gap variations along the growth direction and will show a non-uniform performance due to differences in the amount of charge produced as a function of the photon energy. These various flaws limit the full exploitation of the material, particularly for large ($>1\,cm^3$) spectrometer grade devices. The yield of such devices is currently only a few percent, which affects their efficiency, cost and availability.

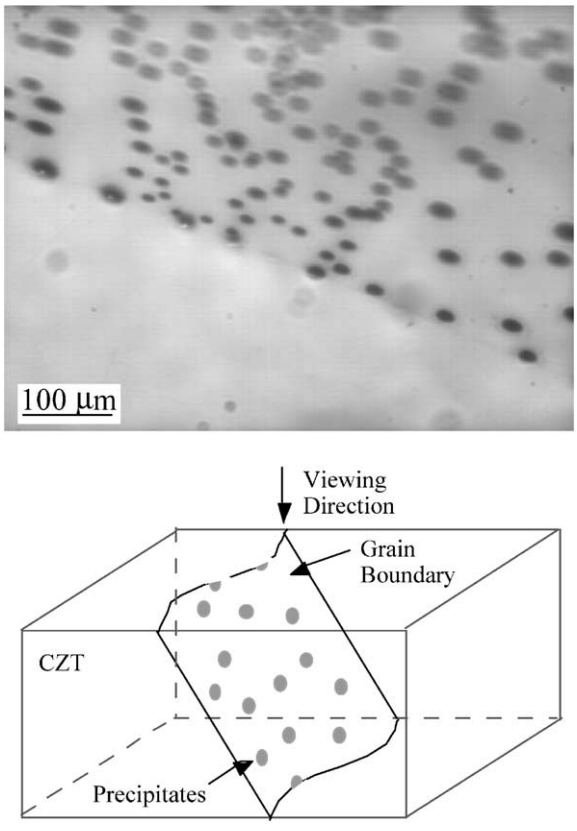

Fig. 1. Infrared transmission micrograph of CZT as seen along a grain boundary.

5. Structural defects characterized by XRD

Structural defects are known to strongly influence the performance of semiconductor devices. Sub grain/twin boundaries are known to lead to high dark current. X-ray diffraction analysis of HPB $Cd_{1-x}Zn_xTe$, which uses double crystal

X-ray diffraction (DCD) technique, cannot separate the effects of peak broadening due to tilt and strain. Doty [9] reported an average DCD FWHM value of 14 arcsec for $Cd_{0.96}Zn_{0.04}Te$, and an average etch pit density of $1 \times 10^4\,cm^{-2}$. DCD studies showed values for the FWHM ranging from ~20 to 120 arcsec on HPB CdTe crystals [30]. However, neither study reported a clear relationship between the X-ray diffraction results and detector performance. This may be due to the fact that the FWHM measured by the DCD technique includes the effects of both lattice tilt and lattice strain. Surface quality can also play a role. In general, the FWHM values obtained by the DCD technique do not necessarily represent the true crystal quality, because the values do not accurately measure the amount of lattice tilt. By using triple axis diffraction, (TAD), the effects of both mosaicity and strain can be clearly discerned. A correlation between the TAD, etch pit densities, and nuclear detector performance has been observed [31]. Three examples of TAD ω-scans are summarized in Table 3, which illustrate the various features of the ω-scans [29].

The FWHM of the ω-scan, which reveals the tilt boundary, is measured as the angular separation between the half intensity of the left peak and the half intensity of the right peak. As a comparison, under the same experimental conditions, a typical silicon crystal exhibits a single narrow peak with an FWHM = 3.5 arcsec based on the (0 0 4) reflection.

The variations in the crystal quality as indicated by the FWHM values are presumed to stem from the non-optimal thermal stress induced during crystal growth and cool down. If this is indeed the case, the crystallinity variation "pattern" measured from the surface (several microns depth) are likely to project through the thickness of the sample (~2.5 mm thick). This was verified by performing the TAD ω-scan measurements after repeatedly etching away ~100 μm of material, as well as measuring both the front and backsides of the crystals. The results indeed showed the crystallinity variation pattern to project through the thickness of the crystal. The authors would like to point out that the surface processing can also affect the TAD and DAD results, and care must be taken to carefully polish the surfaces before each XRD measurement.

Although the TAD ω-scan mapping provides a great deal of information, the spatial distribution of the crystalline quality can be measured more precisely by double crystal X-ray topography [32]. A combination of these two techniques provides an even more powerful means to characterize the crystalline perfection of single crystal wafer regions. The double crystal X-ray topography can identify the locations of tilt boundaries and delineate sub-grains within single crystalline CZT, as seen in Fig. 2. The two topographs (white = diffracted intensity) labeled A and B were taken at the top of the two peaks shown in the rocking curve. The two sub-grains as indicated in the figure are separated by 130 arcsec (0.0361°). Locations of tilt boundaries are also indicated by arrows and the results are consistent with the TAD ω-scan FWHM mapping, which is also shown in the figure.

Since dislocations induce local lattice tilting, the broadening of the TAD ω-scans in regions of low crystal quality can be attributed to the presence of dislocations. Furthermore, this correlation has the implication that the TAD ω-scans can be used as a non-destructive tool (as opposed to the EPD measurements) to uniquely assess the crystalline perfection of $Cd_{1-x}Zn_xTe$. However, it is difficult to use TAD scans to rapidly screen a large number of wafers during detector manufacturing due to the time required to study each sample.

Table 3
Summary descriptions of the three TAD ω-scans

TAD ω-scan representing:	FWHM (arcsec)	Characteristic feature
(A) High crystal quality	8	Single, narrow peak
(B) Tilt boundary	50	Two (or more) resolvable peaks
(C) Mosaic structure	45	Single, broadened peak

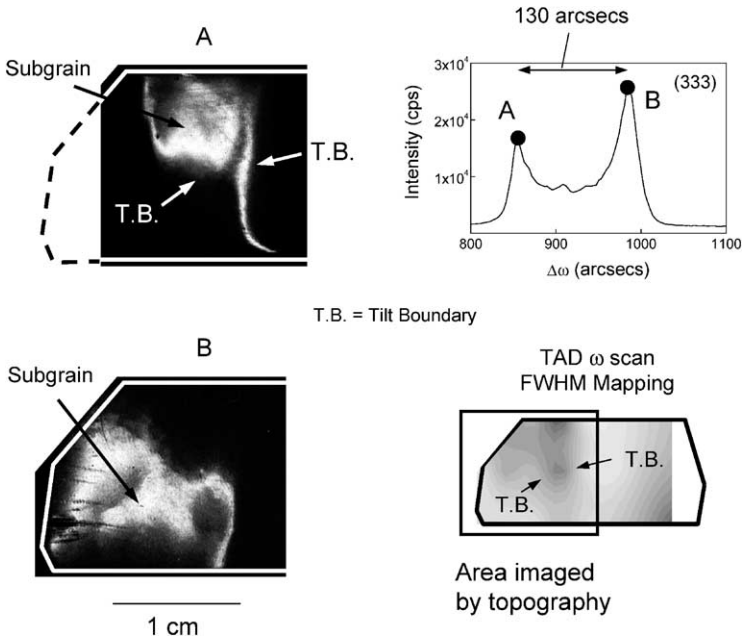

Fig. 2. Double axis X-ray topographs (white = diffracted intensity) of a single crystal $Cd_{1-x}Zn_xTe$. The two exposures, A and B, were taken at the top of the two peaks shown in the rocking curve.

6. Defects characterized by low-temperature photoluminescence (PL) spectroscopy

A typical 4.2 K PL spectrum for $Cd_{1-x}Zn_xTe$ is shown in Fig. 3. It consists of several regions: (1) near-band-edge region, consisting of free and bound exciton peaks; (2) donor–acceptor region, consisting of a (D,A) transition and its first two phonon replicas; the phonon replicas of the excitonic luminescence also lie in this region; (3) a defect band centered at 1.4 eV due to the A-center, which is a Cd vacancy in complex with a donor; and (4) a band centered at 1.1 eV believed to be related to tellurium vacancies.

Region (i), the near-band-edge region, contains some of the most useful information in the low-temperature PL spectrum. Fig. 4 shows the near-band-edge spectrum for an especially high-quality $Cd_{1-x}Zn_xTe$ sample with $x \approx 0.1$. The dominant peak is the donor-bound exciton (D^0, X), in contrast to CdTe and $Cd_{0.96}Zn_{0.04}Te$, where (A^0, X) is typically dominant. A ground state-free exciton peak ($X_{n=1}$ or X_1), upper polariton band (X_{up}) and first excited state free exciton ($X_{n=2}$ or X_2) are also visible. Because of the greater degree of alloy broadening for $x = 0.1$ compared to $x = 0.04$, the free exciton peak is barely resolvable from the donor-bound exciton in this case; in poorer quality material the two peaks are not resolvable at all.

The low-temperature PL spectrum gives an excellent overall picture of material quality, and it is natural to expect that it would be valuable as a predictor of detector performance. The PL spectra for a high-quality detector is dominated by the excitonic luminescence, while that of a poor-quality sample is dominated by defect-related luminescence. Another indicator, which is not obvious, is the sharpness of the spectrum, that is, the extent to which adjacent peaks can be resolved. A third indicator which applies to CZT and which is not well understood is that in high-quality samples the donor-bound exciton (D^0, X) peak tends to be dominant, while in lower-quality samples the acceptor-bound exciton (A^0, X) luminescence is stronger. This observation is probably due to the relatively large number of donors compared to acceptors in the higher-quality

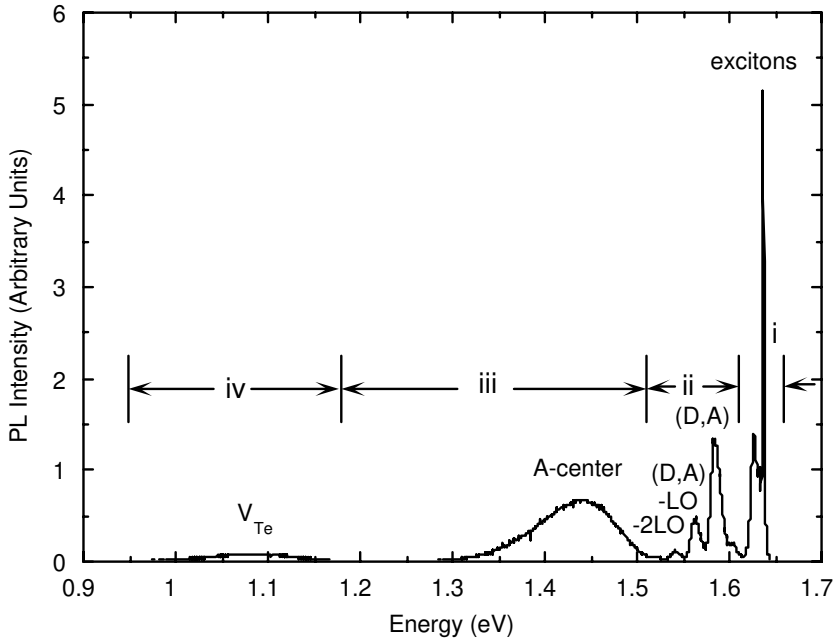

Fig. 3. Representative 4.2 K photoluminescence spectrum for $Cd_{1-x}Zn_xTe$ with $x \sim 0.1$. This spectrum includes (i) excitonic luminescence, (ii) donor-acceptor transitions and (iii) a defect band due to the A-center (Cd vacancy), and (iv) a defect band (related to Te vacancy).

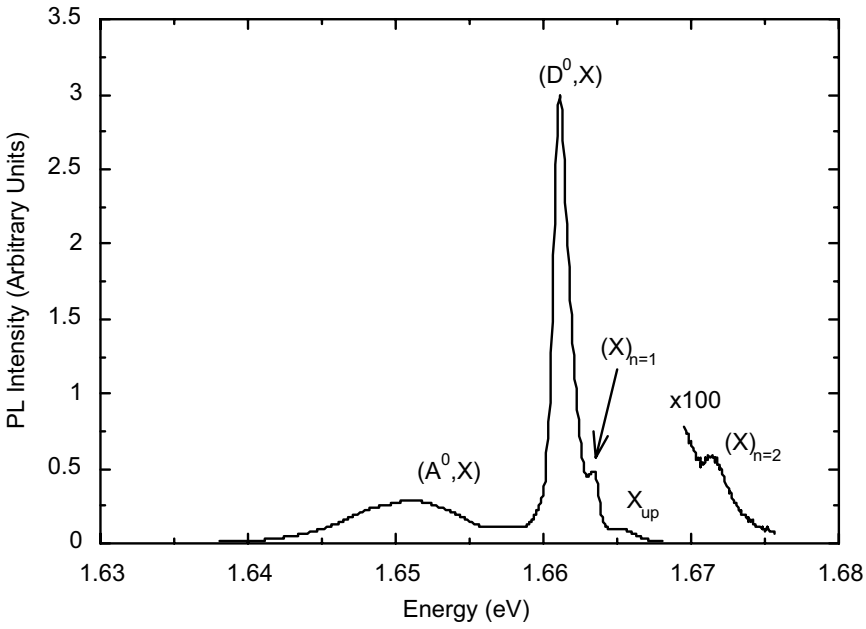

Fig. 4. Near-band-edge PL spectrum for a high-quality $Cd_{1-x}Zn_xTe$ sample with $x \sim 0.1$.

material, together with the beneficial role the donors can play to increase the electrical resistivity and alter the trapping centers due to the formation of complexes.

7. Nuclear spectroscopic spectra

Most of the nuclear detector studies have been dedicated to CZT grown by vertical HPB, which is a stable commercial product. However, recently low-pressure Bridgman crystals have been grown and evaluated in both the horizontal and vertical geometries [28]. It appears that the carrier lifetimes of the low-pressure CZT are now comparable to HPB samples and may soon become superior to HPB samples, particularly for large area devices [26]. Table 4 shows a comparison of results.

Table 4
TAD XRD ω and $\theta/2\theta$ scans and nuclear spectroscopic response obtained on two high-pressure and three low-pressure Bridgman CZT

	HPB		LPB		
	USA-1	Ukraine	USA-1	USA-2	Israel
FWHM ω-scan	10	16	14	16	24
FWHM $\theta/2\theta$ scan	30	54	30	54	17
FWHM ^{57}Co	12.9%	20%	12.0%	3%	12.5%

One can see that the results start to be comparable. Nevertheless, when it comes to large production capability the HPB method has the advantages of being more mature, more furnaces in operation for producing gamma detectors, and better control of the Cd loss. The low-pressure techniques have the advantage of much larger crystals ($>100\,cm^3$) and potentially a higher yield.

Fig. 5 shows the ^{57}Co spectra of the two HPB detectors listed in Table 4. One can see that even the HPB sample from the Ukraine, which has a much higher level of impurities still makes a reasonable detector. The vapor-grown crystals, which have a degree of purity that is 1–2 orders of magnitude better than the Ukrainian sample did not produce detector grade crystals.

8. Conclusions

The present review shows the importance of finding the right methods to characterize CZT for their use as nuclear detectors. Due to the large amount of potential market for the detectors, it explains the need to better elucidate the role of point defects, extended defects, and stoichiometry deviations, and to understand the optimal choice of growth and post-growth annealing conditions to minimize the effects of deleterious carrier traps.

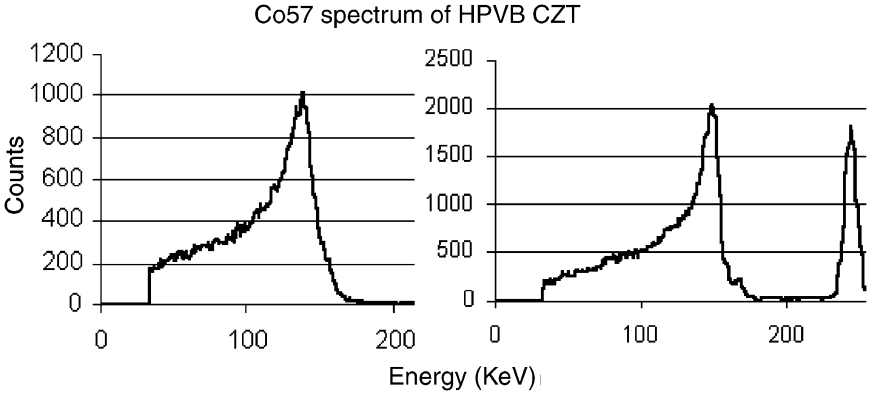

Fig. 5. Nuclear spectroscopic spectrum of ^{57}Co for sample HPB-Ukraine (left), and HPB-USA-1 (right), the peak on the far right is a pulser.

References

[1] T.E. Schlesinger, J.E. Toney, R.B. James, L. Franks, H. Yoon, Mater. Sci. Eng. Rep. 32 (4-5) (2001) 103.
[2] R. Lauer, F. Williams, J. Appl. Phys. 42 (1971) 2904.
[3] W. Trower, Mater. Res. Soc. Symp. Proc. 487 (1988) 19.
[4] T.-C. Yu, R.F. Brebrick, J. Phase Equilibria 13 (1992) 476.
[5] R. Triboulet, G. Neu, B. Fotouhi, J. Crystal Growth 65 (1983) 263.
[6] P. Chevnart, U. El-Hanani, D. Schneider, R. Triboulet, J. Crystal Growth 101 (1990) 270.
[7] M. Bruder, H. Schwarz, R. Schmitt, H. Maier, J. Crystal Growth 101 (1990) 266.
[8] J.F. Butler, F.P. Doty, C. Lingren, Proc. SPIE 1734 (1992) 131.
[9] F.P. Doty, J.F. Butler, J.F. Schetzina, K.A Bowers, J. Vac. Sci. Technol. B 10 (1992) 1418.
[10] C. Szeles, E.E. Eissler, MRS Symp. Proc. 487 (1998) 3.
[11] C. Szeles, M. Driver, SPIE Proc. 3446 (1998) 2.
[12] E. Raiskin, J. Butler, IEEE Trans. Nucl. Sci. 35 (1988) 81.
[13] H. Hermon, M.M. Schieber, M.S. Goorsky, T.T. Lam, E. Meerson, H.W. Yao, J.C. Erickson, R.B. James, in: R.B. James, R.C. Schirato (Eds.), Hard X-ray, Gamma-Ray and Neutron Detector Physics II, Vol. 4141, SPIE, Bellingham, WA, 2000, p. 186.
[14] R.B. James, T.E. Schlesinger, J. Lund, M. Schieber, in: T.E. Schlesinger, R.B. James (Eds.), Semiconductors for Room Temperature Nuclear Detector Applications Semiconductors and Semimetals Series, Vol. 43, Academic Press, New York, 1995, p. 335.
[15] H. Hermon, M. Schieber, R.B. James, N.N. Kolesnikov, Yu.N. Ivanov, V. Komar, M.S. Goorsky, H. Yoon, J. Toney, T.E. Schlesinger, in: R.B. James, T. E. Schlesinger, P. Siffert, W. Dusi, M. Squillante, M. O'Connell, M. Cuzin (Eds.), Vol. 487, Materials Research Society, Pittsburgh, PA, 1998, 223.
[16] N.N. Kolesnikov, A.A. Kolchin, D.L. Alov, Yu.N. Ivanov, A.A. Chernov, M. Schieber, H. Hermon, R.B. James, M.S. Goorsky, H. Yoon, J. Toney, B. Brunett, T.E. Schlesinger, J. Crystal Growth 174 (1997) 256.
[17] M. Schieber, H. Hermon, R.B. James, J. Lund, A. Antolak, D. Morse, N.N. Kolesnikov, Yu.N. Ivanov, M.S. Goorsky, J.M. Van Scyoc, H. Yoon, J. Toney, T.E. Schlesinger, F.P. Doty, IEEE Trans. Nucl. Sci. 4 (1997) 2566.
[18] M. Schieber, H. Hermon, R.B. James, J. Lund, A. Antolak, D. Morse, N.N. Kolesnikov, Yu.N. Ivanov, M.S. Goorsky, H. Yoon, J. Toney, T.E. Schlesinger, Proc. SPIE 3115 (1997) 305.
[19] H. Hermon, M. Schieber, R.B. James, J. Lund, A. Antolak, D.H. Morse, N.N.P. Kolesnikov, Yu.N. Ivanov, V. Komar, M.S. Goorsky, H. Yoon, J. Toney, T.E. Schlesinger, in: R.B. James, T.E. Schlesinger, P. Siffert, W. Dusi, M. Squillante, M. O'Connell, M. Cuzin (Eds.), Semiconductors for Room Temperature Radiation Detector applications II, Vol. 487, Materials Research Society, Pittsburgh, PA, 1998, p. 13.
[20] H. Hermon, M. Schieber, R.B. James, A.J. Antolak, D. Morse, B. Brunett, C. Hackett, E. Tarver, V. Komar, M.S. Goorsky, H. Yoon, N.N. Kolesnikov, J. Toney, T.E. Schlesinger, Nucl. Instrum. Methods A 428 (1999) 30.
[21] E.Y. Lee, B.A. Brunett, R.W. Olsen, J.M. Van Scyoc, H. Hermon, R.B. James, Proc. SPIE 3446 (1998) 40.
[22] James, R.B., Schlesinger, T.E., in: T.E. Schlesinger, R.B. James (Eds.), Semiconductors for Room Temperature Nuclear Applications, Vol. 43, Academic Press, New York, 1995, p. 335 (Chapter 9).
[23] M. Muhlberg, P. Rudolph, C. Genzel, B. Wermke, U. Becker, J. Crystal Growth 101 (1990) 275.
[24] M. Muhlberg, P. Rudolph, C. Genzel, B. Wermke, U. Becker, J. Crystal Growth 101 (1990) 275.
[25] T.E. Schlesinger, M. Greaves, S. Ross, B.A. Brunett, J.M. Van Scyoc, R.B. James, in: R.B. James, R.C. Schirato (Eds.), Hard X-ray, Gamma-Ray, and Neutron Detector Physics and Applications, Vol. 3768, SPIE, Bellingham, WA, 1999, p. 16.
[26] Y. Nemirovsky, A. Peyser, J. Gurelik, R.B. James, H.W. Yao, Longxia Li, F. Lu, J. Electron. Mater., in press.
[27] Doty, F.P., Presented at 1998 US Workshop on the Physics and Chemistry of II–VI Semiconductors, Charleston, SC, October 21–22, 1998.
[28] M. Schieber, R.B. James, H. Hermon, A. Vilensky, I. Baydjanov, M. Goorsky, T. Lam, E. Meerson, H.W. Yao, J. Erickson, E. Cross, A. Burger, J.O. Ndap, G. Wright, M. Fiederle, J. Crystal Growth, accepted for publication.
[29] R.B. James, B. Brunett, J. Heffelfinger, J. Van Scyoc, J.C Lund, F.P. Doty, C.L. Lingren, R. Olsen, E. Cross, H. Hermon, H. Yoon, N. Hilton, M. Schieber, E.Y. Lee, J. Toney, T.E. Schlesinger, M. Goorsky, W. Yao, H. Chen, A. Burger, J. Electron. Mater. 27 (1998) 788.
[30] E.J. Johnson, J.A. Kafalas, R.W. Davies, J. Appl. Phys. 54 (1982) 204.
[31] H. Yoon, S.E. Lindo, M.S. Goorsky, J. Crystal Growth 174 (1997) 775.
[32] H. Yoon, J.M. Van Scyoc, T.S. Gilbert, M.S. Goorsky, B.A. Brunett, J.C. Lund, H. Hermon, M. Schieber, R.B. James, Mater. Res. Soc. Symp. Proc. 487 (1998) 115.